Prospects for detecting individual defect centers using spatially resolved electron energy loss spectroscopy

David Kordahl,[1] Lance W. Q. Xu,[1] Shery L. Y. Chang,[2] and Christian Dwyer[1,*]
[1]*Department of Physics, Arizona State University, Tempe, Arizona 85287, USA*
[2]*Eyring Materials Center and School of Molecular Sciences, Arizona State University, Tempe, Arizona 85287, USA*

(Received 21 July 2019; published 14 October 2019)

We consider the prospects of locating and characterizing individual defect centers in bulk materials using electron energy loss spectroscopy (EELS) in a scanning transmission electron microscope (STEM). We simulate STEM-EELS maps for two important defect centers in diamond, namely, the negatively charged nitrogen-vacancy defect and the neutral silicon-vacancy defect. We use density-functional theory to compute the defect electronic structure and a Møller potential formalism to compute the inelastic electron scattering. Our results indicate that it should be possible to use STEM-EELS to obtain the transverse locations of these defects to within about 1 nm. We calculate the plane-wave scattering cross sections for these individual defects to be of the order of 10^{-4} Å^2, which indicates that the EELS signals should be within detectable limits. Calculated spectral maps and scattering cross sections are given as a function of the defect orientation, and we show that the results can be interpreted using a tight-binding description of the defect electronic structure.

DOI: 10.1103/PhysRevB.100.134103

I. INTRODUCTION

Our ability to probe the atomic and electronic structures of individual point defects embedded in materials remains one of the last frontiers in materials characterization. Whereas interfaces (two-dimensional defects) and dislocation lines (one-dimensional defects) have been well studied at the atomic level, the small volumes and weak signals associated with individual point defects (zero-dimensional defects) make their detection intrinsically challenging. Over the last decade, the analysis of individual heavy dopant atoms within bulk materials using annular dark field imaging in a scanning transmission electron microscope (ADF-STEM) has seen significant progress [1–6]. ADF-STEM has also been combined with the detection of characteristic x rays to locate and unambiguously identify dopant atoms in carbon materials [7]. There has also been progress in imaging lighter dopants or vacancies embedded in lower-dimensional materials [8,9]. But locating lighter dopants or vacancies in three-dimensional (3D) materials remains extremely difficult. Nevertheless, point defects of the latter type are crucial to the operation of many semiconductors, quantum computing materials, quantum sensing materials, oxygen and hydrogen storage materials, etc. Highly relevant examples include color centers in diamond and silicon carbide, where light atoms such as nitrogen or silicon paired with lattice vacancies form defect centers that can emit light upon the decay of an excited state. The optical and spin properties of these defect centers find application in quantum computing and nanoscale sensing. Locating and characterizing such defect centers typically relies on optical-based techniques such as photoluminescence, where the spatial resolution is usually diffraction limited by the wavelength of the light, and hence the properties of the defect centers are typically measured as ensembles. However, ongoing efforts to improve the performance of both individual and ensembles of defect centers for quantum information and sensing are driving the development of new characterization techniques that aim to achieve higher spatial resolution. Hence the ability to locate individual occurrences of such point defects with high precision and to probe their electronic states and their crystallographic environments with high spatial and energy resolutions would be immensely valuable to many physicists, materials scientists, and chemists.

Electron energy loss spectroscopy (EELS) provides a way to detect point defects via their characteristic spectroscopic signals, allowing the study both of point defects that emit light and of those that do not (dark modes). Crucially, EELS does not require the atomic number of a point defect to differ greatly from that of the atoms surrounding it, making this technique applicable to important points defects such as nitrogen-vacancy (NV) centers in diamond. Using EELS, point defects have already been located at submicron levels, like with the characterization of NV concentrations in nanodiamonds [10] and reports of poorly understood defects in BAlN thin films [11]. On the other hand, we expect that the EELS signal (or any spectroscopic signal) associated with any *individual* point defect to be very weak. Moreover, apart from the weak signals, a grand challenge in detecting individual point defects via EELS is the degree of spatial delocalization given by v/ω: since it is inversely proportional to the energy loss $\hbar\omega$, the resolution of spatial mapping becomes poor ($\sim$10 nm) for the excitation energies of interest ($\sim$1 eV).

Here we analyze the prospects of using STEM-EELS to locate individual point defects in 3D materials and to probe their electronic signatures. As case studies, we consider the negatively charged nitrogen-vacancy (NV^-) center in diamond, with a zero-phonon transition energy of $\sim$1.9 eV, and

*christian.dwyer@asu.edu

the charge-neutral silicon-vacancy (SiV^0) center in diamond, with a zero-phonon transition energy of ∼1.3 eV. The NV^- center has been studied for half a century [12], but continued interest is spurred by its relevance as a room-temperature qubit with well-established readout procedures [13,14]. When the robust spin coherence of SiV^0 is considered alongside advances in production and initialization [15,16], it also emerges as a strong candidate for quantum information applications [17]. Both defects show promise as single-photon emitters to be used as building blocks in quantum information science, quantum sensing, and metrology. We use density-functional theory (DFT) to model the electronic structures of these defects and apply the resulting wave functions to predict the corresponding STEM-EELS maps. With this approach, we are able to compute STEM-EELS maps for different defect orientations, and we find plane-wave cross sections on the order of 10^{-4} Å^2 and feasible spatial localization on the order of 1 nm. As we will show, the STEM-EELS maps of these defects can be intuitively understood using a tight-binding description.

Our paper has the following order. First, we review the theory of STEM-EELS (Sec. II) and describe our methods (Sec. III). Then electronic structures are reviewed and spectral maps are presented for NV^- (Sec. IV) and SiV^0 (Sec. V). These results are discussed (Sec. VI) before we conclude.

II. THEORY OF STEM-EELS

We use a Møller potential formalism [18–20] to calculate the probability of inelastic scattering of STEM beam electrons which excite a defect center. For a defect electronic transition $\varphi_0 \rightarrow \varphi_n$, the Møller potential (strictly a potential energy) is given by

$$V_n(x) = e^2 \int d^3x' \, \frac{\bar{\varphi}_n(x')\varphi_0(x')}{|x - x'|}. \tag{1}$$

It is convenient to consider the quantity $-e\bar{\varphi}_n\varphi_0$ as a charge density, albeit a complex one, which we refer to as the transition charge:

$$\rho_n(x) = -e\bar{\varphi}_n(x)\varphi_0(x). \tag{2}$$

The Møller potential simply describes the instantaneous Coulomb interaction between the beam electron and the transition charge ρ_n. Note that we are using nonrelativistic theory in that retardation and magnetic interactions are ignored, although we do use the relativistic expressions for the mass and wavelength of the beam electrons when needed.

To calculate the inelastic scattering of beam electrons, we adopt the projection approximation and assume that the inelastic scattering is improbable enough that it is accurately described by a first-order interaction. Under these approximations, the inelastic scattering can be regarded as taking place within a plane coinciding with the point defect and perpendicular to the optic axis $\hat{\mathbf{z}}$. In this plane, the wave function describing beam electrons in the nth inelastic channel is given by

$$\psi_n(\mathbf{x}) = -\frac{i}{\hbar v} V_n(\mathbf{x})\psi_0(\mathbf{x}), \tag{3}$$

where v is the speed of the beam electrons, $V_n(\mathbf{x})$ is the projected Møller potential defined below, and ψ_0 is the wave function for the elastic channel.

The projected Møller potential is defined as

$$V_n(\mathbf{x}) = \int_{-\infty}^{\infty} dz \, V_n(x) e^{i\omega_n z/v}, \tag{4}$$

where $\hbar\omega_n$ is the energy loss. The projected Møller potential is conveniently calculated via Fourier space

$$V_n(\mathbf{x}) = \int \frac{d^2\mathbf{q}}{(2\pi)^2} \tilde{V}_n(\mathbf{q}) e^{i\mathbf{q}\cdot\mathbf{x}}, \tag{5}$$

where

$$\tilde{V}_n(\mathbf{q}) = -\frac{4\pi e\tilde{\rho}_n(\mathbf{q})}{\mathbf{q}^2 + \omega_n^2/v^2}. \tag{6}$$

In this expression, $\tilde{\rho}_n$ is the Fourier transform of the projected transition charge density

$$\tilde{\rho}_n(\mathbf{q}) = \int d^2\mathbf{x} \, \rho_n(\mathbf{x}) e^{-i\mathbf{q}\cdot\mathbf{x}}, \tag{7}$$

with the projected transition charge density itself being defined by

$$\rho_n(\mathbf{x}) = \int_{-\infty}^{\infty} dz \, \rho_n(x) e^{i\omega_n z/v}. \tag{8}$$

For STEM-EELS, the elastic wave function ψ_0 is that of a focused beam. The strength of the EELS signal corresponds to the probability that beam electrons will be scattered inelastically and admitted by the EELS collection aperture in the diffraction plane. This probability is calculated by integrating the squared modulus of the Fourier transform of the inelastic wave function over those wave vectors admitted by the collection aperture. In general, the inelastic wave function will undergo elastic scattering from the atoms in the sample downstream from the defect plane before reaching the diffraction plane. However, for simplicity we neglect elastic scattering of the beam electrons and further presume that all inelastically scattered electrons are collected. The relatively large inelastic delocalization length v/ω and the consequent nanometer, rather than atomic-scale, spatial resolution mean that these simplifications do not significantly affect our conclusions in what follows.

III. METHODS

Our DFT calculations were performed using the Vienna Ab initio Simulation Package (VASP) [21–24]. We used a $4 \times 4 \times 4$ conventional supercell ($4^3 \times 8 - 1 = 511$ atoms) with Γ-point sampling and a 420-eV cutoff. Projector augmented-wave pseudopotentials were used [25,26] under the generalized gradient approximation [27]. Excited states were calculated using an occupation constraint, as discussed below. The pseudized wave functions in this approach match the all-electron wave functions outside the atomic cores where the pseudopotentials are deployed, so we expect the wave functions for the defect states to accurately describe the defect states as independent electron states, localized as they are in the vacancy regions.

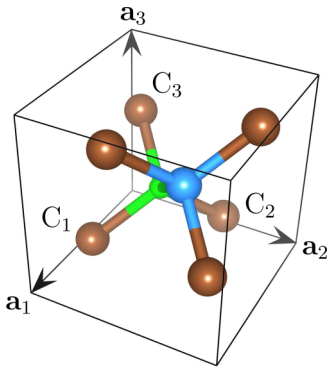

FIG. 1. The atomic structure of the NV center in diamond (carbon atoms are brown, the nitrogen atom is blue, and vacancy is green). Carbon atoms immediately adjacent to the vacancy are labeled $C_{1,2,3}$. (This visualization, as well as the isosurface plots, was built using VESTA [30]).

We constructed real-space electron wave functions on a 3D grid using Fourier coefficients extracted via WAVETRANS [28]. The wave functions output by VASP were initially complex valued but were made real valued by similarity transformations among degenerate states (see the Appendix). These symmetrized wave functions were used to compute the real-space transition charges [Eq. (2)]. Using the 3D transition charge densities, we calculated the projected transition charge densities on a 2D grid [Eq. (8)], padded the grid as needed for convergence, and Fourier transformed the results to construct the **q**-space projected Møller potentials [Eq. (6)]. Inverse Fourier transformation yielded the projected Møller potentials in real space [Eq. (5)]. Since the dielectric function for diamond is fairly flat for the frequencies of interest [29], we incorporated screening by dividing the projected Møller potentials by the static dielectric constant.

IV. THE NV$^-$ DEFECT CENTER

This section contains our results for the NV$^-$ defect center in diamond. This defect consists of a substitutional nitrogen atom immediately adjacent to a carbon vacancy, with the defect carrying an additional electron, making it negatively charged. For definiteness we choose the N-V axis to lie along the [111] crystallographic direction of the (nonprimitive) fcc diamond unit cell, as in Fig. 1.

A. Electronic structure of NV$^-$

The electronic structure and excited states of the 1.945 eV transition of the NV$^-$ center have been extensively characterized, from both the directions of molecular-orbital and group theoretic analysis [31–33] and of DFT [34–36], with recent DFT analyses going so far as to incorporate the vibrational [37–39] and surface [40] effects. Later, we will use DFT wave functions to calculate the EELS scattering probabilities based on the theory outlined in Sec. II. But first, we review the electronic structure of the NV$^-$ defect from a tight-binding perspective. The tight-binding approximation yields results that are less accurate than those of DFT, but these results give us physical insights that guide our interpretation.

For the tight-binding description, let $c_{1,2,3}$ denote the dangling bond orbitals from the three carbon atoms $C_{1,2,3}$ immediately adjacent to the vacancy, as labeled in Fig. 1, and let n denote the dangling bond orbital from the N atom. Assuming no overlap between dangling bond orbitals, we can form the following mutually orthogonal symmetry-adapted orbitals for the C_{3v} point group of the NV$^-$ defect:

$$\begin{pmatrix} a_1(1) \\ a_1(2) \\ e_x \\ e_y \end{pmatrix} = \begin{pmatrix} \alpha/\sqrt{3} & \alpha/\sqrt{3} & \alpha/\sqrt{3} & \beta \\ -\beta/\sqrt{3} & -\beta/\sqrt{3} & -\beta/\sqrt{3} & \alpha \\ 1/\sqrt{2} & -1/\sqrt{2} & 0 & 0 \\ 1/\sqrt{6} & 1/\sqrt{6} & -2/\sqrt{6} & 0 \end{pmatrix} \begin{pmatrix} c_1 \\ c_2 \\ c_3 \\ n \end{pmatrix}, \tag{9}$$

where α denotes the degree of mixing of carbon and nitrogen dangling bonds and $\beta = \sqrt{1-\alpha^2}$ preserves normalization. Each symmetry-adapted orbital can have spin up or spin down. For the NV$^-$ defect, these orbitals are populated by six electrons: three from $C_{1,2,3}$, two from the nitrogen atom, and one excess dopant electron that makes the defect charged.

Figure 2 shows the electronic configurations predicted by DFT [local spin-density approximation (LSDA)] for the ground state and for the optically allowed excited state of interest here. Spin-orbit interactions lift the degeneracy of spin-up and spin-down orbitals, such that the ground state is populated by an excess of spin-up electrons (similar to Hund's rule from atomic theory). The excited state corresponds to the promotion of an electron from $a_1^{\downarrow}(2)$ to $e_x^{\downarrow}$ or $e_y^{\downarrow}$. The excited state is regarded as containing half-occupied $e_y^{\downarrow}$ and $e_y^{\downarrow}$ orbitals, which preserves the C_{3v} symmetry. The excitation preserves electron spin (i.e., there are no spin flips). The LSDA difference in system energy between the constrained excited state and ground state is 1.708 eV, which should be compared with the accepted experimental value of 1.945 eV. The discrepancy of 0.23 eV is typical of such DFT predictions, and apart from slightly affecting the predicted energy position of the NV$^-$ spectral signature, it does not cause any substantial inaccuracy in the present work. The relevant DFT wave functions are also shown in Fig. 2; they qualitatively resemble the symmetry-adapted orbitals given above.

It is also instructive to use the symmetry-adapted orbitals to construct the transition charges $\bar{e}_x a_1(2)$ and $\bar{e}_y a_1(2)$ and their associated dipole moments. Assuming for simplicity that the bond orbitals are completely separated in space, the transition charges have the following simple approximate forms:

$$\begin{aligned} \bar{e}_x a_1(2) &\approx \frac{\beta}{\sqrt{6}}(-|c_1|^2 + |c_2|^2), \\ \bar{e}_y a_1(2) &\approx \frac{\beta}{\sqrt{18}}(-|c_1|^2 - |c_2|^2 + 2|c_3|^2). \end{aligned} \tag{10}$$

For convenience, we introduce $\hat{\mathbf{x}}$ and $\hat{\mathbf{y}}$ perpendicular to the [111] N-V axis and $\hat{\mathbf{z}}$ parallel to it: $\hat{\mathbf{x}} = \frac{1}{\sqrt{2}}[\bar{1}, 1, 0]$, $\hat{\mathbf{y}} = \frac{1}{\sqrt{6}}[\bar{1}, \bar{1}, 2]$, $\hat{\mathbf{z}} = \frac{1}{\sqrt{3}}[111]$. We then use an ansatz for the dipole moments $\mathbf{p}_{1,2,3}$ of the dangling bonds $|c_{1,2,3}|^2$, consisting of parallel component $p_\parallel$ and a perpendicular component $p_\perp$:

$$\begin{aligned} \mathbf{p}_{1,2} &= p_\perp\left(\mp\frac{\sqrt{3}}{2}\hat{\mathbf{x}} - \frac{1}{2}\hat{\mathbf{y}}\right) - p_\parallel\hat{\mathbf{z}}, \\ \mathbf{p}_3 &= p_\perp\hat{\mathbf{y}} - p_\parallel\hat{\mathbf{z}}. \end{aligned} \tag{11}$$

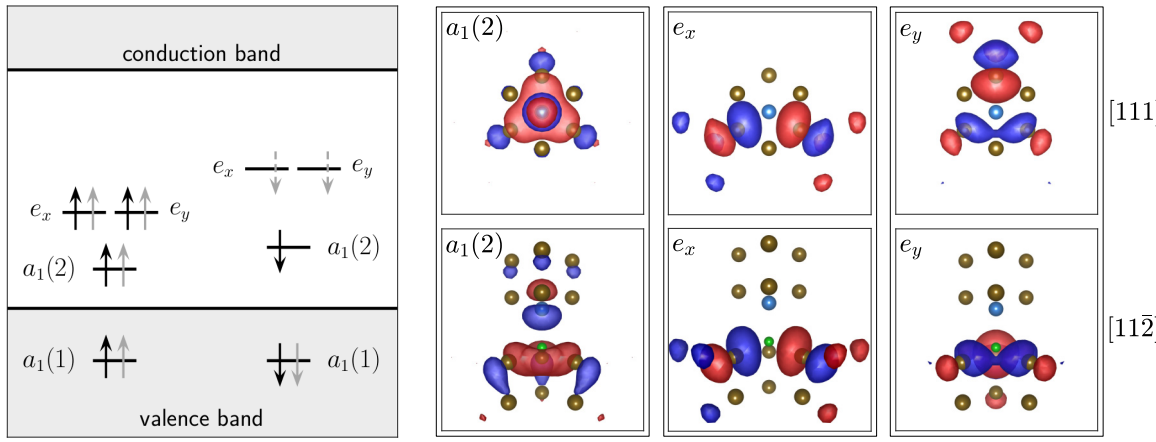

FIG. 2. Left: The DFT (LSDA) predicted ground and excited states of the NV^- defect. Black and gray arrows represent the ground and excited states, respectively, while solid and dashed arrows denote full and half occupancies, respectively. The ground state has a $^3A_2$ (triplet) electronic configuration. The optically allowed excited state is the ^3E (triplet) configuration resulting from single-electron transitions from $a_1^{\downarrow}(2)$ to $e_x^{\downarrow}$ or $e_y^{\downarrow}$ [34]. Right: Isosurface plots of the wave functions involved in the excitation (red is negative; blue is positive), viewed both along and perpendicular to the [111] N-V axis (carbon atoms are brown, the nitrogen atom is blue, and vacancy is green).

Applying this ansatz to Eq. (10), the transition dipole moments adopt especially simple forms given by

$$\begin{aligned}\mathbf{p}(\bar{e}_x a_1(2)) &\approx \frac{\beta}{\sqrt{6}}(-\mathbf{p}_1+\mathbf{p}_2)=\frac{\beta p_\perp}{\sqrt{2}}\hat{\mathbf{x}},\\ \mathbf{p}(\bar{e}_y a_1(2)) &\approx \frac{\beta}{\sqrt{18}}(-\mathbf{p}_1-\mathbf{p}_2+2\mathbf{p}_3)=\frac{\beta p_\perp}{\sqrt{2}}\hat{\mathbf{y}}.\end{aligned} \tag{12}$$

Neither of these dipole moments has a parallel component. Their forms imply that, in the decay of the excited state to the ground state, the NV^- center emits unpolarized photons traveling along the N-V axis.

Figure 3 shows the transition charges formed from the DFT wave functions in Fig. 2. The DFT transition charges show good correspondence with the tight-binding expressions given above. Viewed along the [111] N-V axis, the DFT transition charges possess an obvious dipole character indicative of an optically allowed transition. From the DFT transition charges we find $\beta p_\perp \approx 1.38$ Å, which, for comparison, has the same order of magnitude as that for a hydrogen $1s \leftrightarrow 2p$ transition.

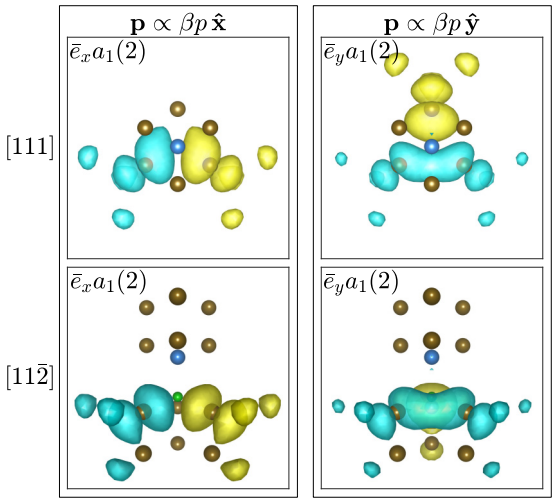

FIG. 3. The two transition charges for the NV^- excitation shown in Fig. 2. Each transition charge is viewed both along and perpendicular to the N-V axis [111], and each has an obvious dipole character indicative of an optically allowed excitation (cyan is negative; yellow is positive).

B. Predictions of NV^- STEM-EELS maps

Figure 4 demonstrates the calculation of the STEM-EELS map of NV^- viewed along the [111] N-V axis. The transition charges in Figs. 4(a) and 4(d) are localized to within a few bond lengths of the defect. By comparison, the Møller potentials Figs. 4(b) and 4(e) extend over about 5 nm, attributable to the inelastic delocalization at this relatively low energy loss (∼1 eV). The STEM-EELS maps exhibit a similar degree of delocalization. It would not be possible to observe the partial STEM-EELS maps in Figs. 4(c) and 4(f), but only in the total map shown in Fig. 4(g) [or Fig. 4(h)], which is the sum of the two partial maps. The total STEM-EELS maps show three symmetric lobes of higher intensity near the center of the defect, corresponding to the positions of the three dangling bonds $c_{1,2,3}$ adjacent to the vacancy. The total map in Fig. 4(h) includes the blurring effect of a Gaussian-shaped STEM probe with 1 Å FWHM.

Figure 5 shows STEM-EELS maps of the NV^- center viewed along three orientations. The three orientations represent a rotation about the $\hat{\mathbf{x}}$ axis defined above, which lies horizontal throughout Fig. 5. In each orientation, the lobes of higher intensity correspond to the dangling bonds $c_{1,2,3}$, as seen in the projection. From the maps we conclude that it is possible in principle to locate the NV^- center transversely to within about 1 nm. An extremely important consideration is the intensity (scattering probability) obtained in the STEM-EELS maps. From Fig. 5 we see that the intensity is approximately 10^{-6} over an area approximately 1 nm^2. Figure 5 also states the cross sections σ for exciting the NV^- center using an incident electron plane wave. The cross sections are the integrals of the map intensities, and they provide convenient

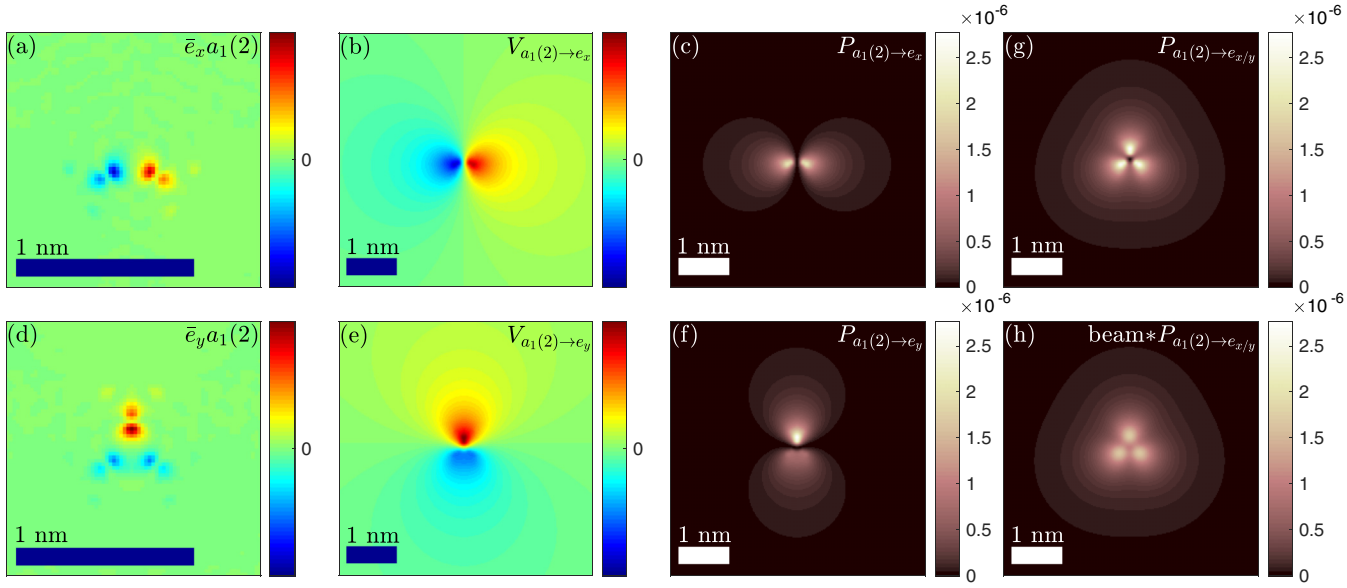

FIG. 4. Calculation of STEM-EELS maps for NV^- viewed along the [111] N-V axis. (a)–(c) Projected transition charge, projected Møller potential, and point-probe STEM-EELS map for transition $a_1^{\downarrow}(2) \to e_x^{\downarrow}$. (d)–(f) Analogous data for transition $a_1^{\downarrow}(2) \to e_y^{\downarrow}$. (g) Total point-probe STEM-EELS map [sum of (c) and (f)] showing threefold rotational symmetry consistent with the C_{3v} point group. (h) Total STEM-EELS map for Gaussian probe with 1 Å FWHM.

measures of the scattering probabilities. The map intensities and plane-wave cross sections are greatest when the defect is viewed along the [111] N-V axis. A detailed discussion of these points will be presented in Sec. VI.

V. THE SiV^0 DEFECT CENTER

This section contains our results for the SiV^0 defect center in diamond. The unusual structure of this defect, shown in Fig. 6, has been recognized since early DFT studies [41]. Unlike the NV center, where the nitrogen atom is only slightly shifted from a carbon position in the undefected structure, SiV^0 adopts a split-vacancy configuration with the silicon atom midway between two vacant sites. This results in a point group symmetry of D_{3d}, which is related to C_{3v} by a direct product with the inversion group: $D_{3d} = C_{3v} \times i$.

A. Electronic structure of SiV^0

The electronic structure of the SiV^0 center has been treated via quantum chemistry [42] and DFT approaches [43,44]. Experimental work in fully characterizing this defect is still ongoing, but recent measurements [45] (correcting an earlier claim [46]) support the identification of the 1.31-eV optically allowed transition as a ${}^3A_{2g} \to {}^3E_u$ transition, matching the DFT prediction [43].

As before, we gain insight into these states from a tight-binding model. Once again letting $c_{1,2,3}$ denote the dangling bond orbitals from the three carbon atoms $C_{1,2,3}$, we must also include $c'_{1,2,3}$ from the three carbon atoms $C'_{1,2,3}$ for this geometry. The full tight-binding treatment would require mixing with the valence orbitals of silicon, but previous investigators [44] have found that the defect states of interest are well described by the carbon orbitals

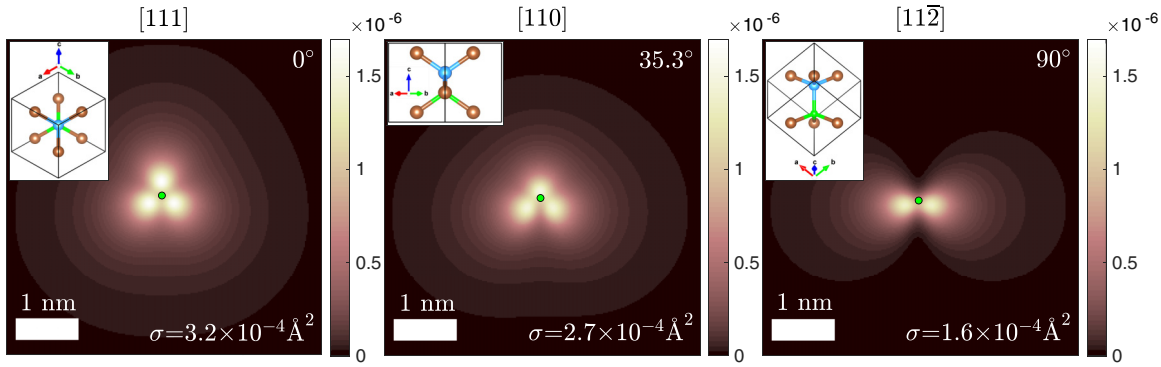

FIG. 5. NV^- in three orientations. STEM-EELS map for Gaussian probe with 1 Å FWHM, viewed along [111], [110], and [11$\bar{2}$], from left to right. The green dot marks the position of the vacancy. The inclination with respect to the [111] N-V axis and the corresponding plane-wave cross section are given in each case.

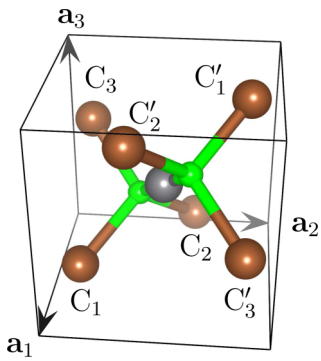

FIG. 6. The atomic structure of the SiV center in diamond (carbon atoms are brown, the silicon atom is gray, and vacancies are green). Carbon atoms $C_{1,2,3}$ are labeled as per the NV center, and carbon atoms $C'_{1,2,3}$ are related to those by inversion about the silicon atom.

alone:

$$
\begin{aligned}
a_{1/2}^{g/u} &= \frac{1}{\sqrt{6}}[(c_1+c_2+c_3)\pm(c'_1+c'_2+c'_3)],\\
e_x^{g/u} &= \frac{1}{2}[(c_1-c_2)\pm(c'_1-c'_2)],\\
e_y^{g/u} &= \frac{1}{\sqrt{12}}[(c_1+c_2-2c_3)\pm(c'_1+c'_2-2c'_3)].
\end{aligned}
\tag{13}
$$

In these expressions, the superscripts g and u denote the gerade and ungerade states, corresponding to the upper and lower signs, respectively. Ten electrons occupy these defect states: six from the carbon orbitals, plus four from the silicon valence, as illustrated by the leftmost panel of Fig. 7. The promotion of fully occupied $e_x^{u\downarrow}$ and $e_y^{u\downarrow}$ states to half-occupied $e_x^{u\downarrow}/e_y^{u\downarrow}$ and $e_x^{g\downarrow}/e_y^{g\downarrow}$ states preserves the D_{3d} symmetry and the electron spin. The DFT prediction for the transition energy is 1.39 eV, which should be compared with the experimental value of 1.31 eV. The relevant wave functions pictured on the right in Fig. 7 qualitatively resemble their tight-binding counterparts.

The transition described above leads to four separate transition charges. But if we assume once again for simplicity that the bonds are separated in space, we find only three *independent* transition charges:

$$
\begin{aligned}
\bar{e}_x^g e_x^u &\approx \frac{1}{4}(|c_1|^2+|c_2|^2-|c'_1|^2-|c'_2|^2),\\
\bar{e}_y^g e_y^u &\approx \frac{1}{12}(|c_1|^2+|c_2|^2+4|c_3|^2-|c'_1|^2-|c'_2|^2-4|c'_3|^2),\\
\bar{e}_x^g e_y^u &\approx \bar{e}_y^g e_x^u \approx \frac{\sqrt{3}}{12}(|c_1|^2-|c_2|^2-|c'_1|^2+|c'_2|^2).
\end{aligned}
\tag{14}
$$

To find the transition dipole moments, we reuse the ansatz of Eq. (11) with the additional stipulation that the dipole moments $\mathbf{p}'_{1,2,3}$ of $|c'_{1,2,3}|^2$ are related to $\mathbf{p}_{1,2,3}$ by inversion, i.e., $\mathbf{p}'_{1,2,3}=-\mathbf{p}_{1,2,3}$. Inserting these expressions into Eq. (10), we find that the dipole moments of $\bar{e}_x^g e_x^u$ and $\bar{e}_y^g e_y^u$ have components along both $\hat{\mathbf{y}}$ and the symmetry axis $\hat{\mathbf{z}}$, while the dipole moments of $\bar{e}_x^g e_y^u$ and $\bar{e}_y^g e_x^u$, equal in this approximation, lie strictly along $\hat{\mathbf{x}}$:

$$
\begin{aligned}
\mathbf{p}(\bar{e}_x^g e_x^u) &\approx (2\mathbf{p}_1+2\mathbf{p}_2)/4 = -\frac{1}{2}p_\perp\hat{\mathbf{y}}-p_\parallel\hat{\mathbf{z}},\\
\mathbf{p}(\bar{e}_y^g e_y^u) &\approx (2\mathbf{p}_1+2\mathbf{p}_2+8\mathbf{p}_3)/12 = \frac{1}{2}p_\perp\hat{\mathbf{y}}-p_\parallel\hat{\mathbf{z}},\\
\mathbf{p}(\bar{e}_y^g e_x^u) &\approx \mathbf{p}(\bar{e}_x^g e_y^u) \approx \frac{\sqrt{3}}{12}(2\mathbf{p}_1-2\mathbf{p}_2) = -\frac{1}{2}p_\perp\hat{\mathbf{x}}.
\end{aligned}
\tag{15}
$$

Figure 8 shows the transition charges formed from the DFT wave functions in Fig. 7. As with the NV^- transition charges, there is an obvious dipole nature to these transition charges when viewed along the [111] Si-V axis. Yet what is strikingly different for the SiV^0 case is that the dipole character of $\bar{e}_x^g e_x^u$ and $\bar{e}_y^g e_y^u$ is even more pronounced when they are viewed along $[11\bar{2}]$, perpendicular to the symmetry axis. Using the DFT transition charges, we find $p_\perp \approx 0.920$ Å and

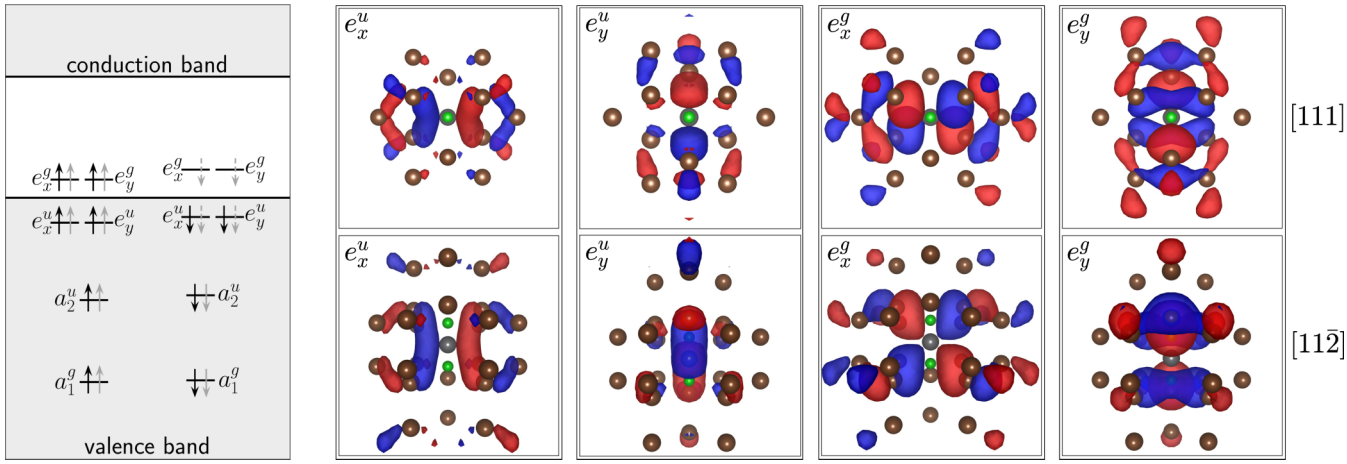

FIG. 7. Left: The DFT (LSDA) predicted ground and excited states of the SiV^0 defect, with arrow conventions following those of Fig. 2. The ground state has a $^3A_{2g}$ (triplet) electronic configuration. The optically allowed excited state is the ^3E_u (triplet) configuration resulting from a single-electron transition from e_x^u or e_y^u to e_x^g or e_y^g [43]. Right: Isosurface plots of the wave functions involved in the excitation (red is negative; blue is positive), viewed both along and perpendicular to the SiV defect axis [111] (carbon atoms are brown, the silicon atom is gray, and vacancy is green).

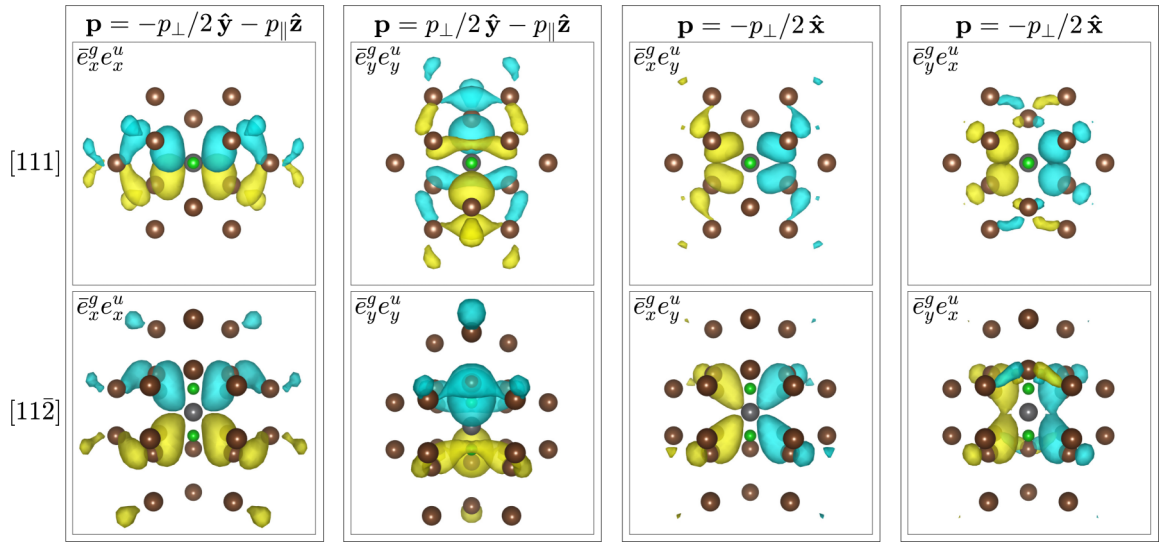

FIG. 8. The four transition charges for the SiV^0 excitation shown in Fig. 7. Each transition charge is viewed both along and perpendicular to the SiV defect axis [111], and like the NV$^-$ excitation, each has an obvious dipole character indicative of an optically allowed excitation (cyan is negative; yellow is positive).

$p_\parallel \approx 0.853$ Å, consistent among all the transitions. Again, these dipole moments have the same order of magnitude as that for a $1s \leftrightarrow 2p$ transition in hydrogen.

As we discuss below, the fact that $p_\parallel > p_\perp/2$ is significant to the character of spectral maps obtained at different orientations. We also note that the $p_\perp$ calculated for the SiV^0 defect is inconsistent with the $p_\perp$ calculated from the NV$^-$ defect, highlighting the quantitative limitations of the tight-binding analysis.

B. Predictions of SiV^0 STEM-EELS maps

Figure 9 shows STEM-EELS maps for the SiV^0 defect along three orientations. As with the NV$^-$ case in Fig. 5, the maps in Fig. 9 indicate that it is possible in principle to locate the defect to within about 1 nm. But the SiV^0 maps are distinct from those of the NV$^-$ case. At the [111] orientation the SiV^0 map exhibits a sixfold rotational symmetry consistent with its D_{3d} point group. At the [11$\bar{2}$] orientation, the SiV^0 map exhibits two vertical lobes along the defect axis arising from the dipole component along that axis, which is in contrast to the lobes along $\hat{\mathbf{x}}$ for the NV$^-$ case. The SiV^0 map intensities and cross sections tend to be smaller than those for NV$^-$, but the same order of magnitude. Moreover, as SiV^0 is rotated away from the defect axis, the plane-wave cross section increases, whereas under the equivalent rotation the plane-wave cross section for NV$^-$ decreases.

VI. DISCUSSION

A key conclusion from the results in Figs. 5 and 9 is that it is possible in principle to use STEM-EELS to locate individual defect centers transversely to within about 1 nm. Such precision is well beyond that permitted by the diffraction limit in photodetection. We compare this precision to the recent nanoscale characterization of the NV$^-$ charge environment by microwave spectroscopy [47], which claimed the localization of a positive charge to within 2 nm of a NV$^-$ center by inference from orientation-specific measurements, without the ability to localize the NV$^-$ defect itself. The

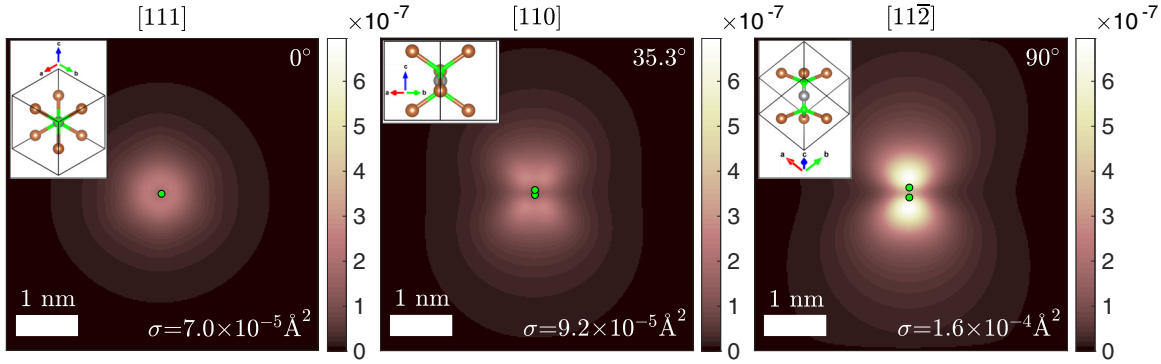

FIG. 9. SiV^0 in three orientations. STEM-EELS maps for Gaussian probe with 1 Å FWHM, viewed along [111], [110], and [11$\bar{2}$], from left to right. The green dots mark the position of the split vacancy. The inclination with respect to the [111] defect axis and the corresponding plane-wave cross sections are given for each case.

STEM-EELS claim of 1-nm precision is consistent with the inelastic delocalization v/ω that determines the upper bound on the impact parameter at which a passing beam electron can cause an excitation [48]. A precision of 1 nm would also enable the crystallographic environment of the point defect to be characterized using STEM imaging.

Another important consideration is whether the scattering probabilities in Figs. 5 and 9 would allow the detection of single-defect centers with a beam electron dose that the sample could tolerate. For the NV^- and SiV^0 excitations considered here, the cross sections for 60-keV plane-wave electrons are in the ranges $1.6–3.2 \times 10^{-4}$ and $0.7–1.6 \times 10^{-4}$ Å^2, depending on orientation. By comparison, the cross section for 60-keV plane-wave electrons to excite the C K shell of a single carbon atom to within a 10-eV energy window immediately above the ionization threshold (285 eV) is 2×10^{-5} Å^2. Compared with this common core-level excitation, the NV^- and SiV^0 cross sections are 5–15 times larger. Given this comparison and the fact that EELS experiments have already detected single atoms via their core-level excitations [9,49,50], our results indicate that detecting single-defect centers such as NV^- and SiV^0 with STEM-EELS is within reach. Recent improvements in electron detection also enhance the experimental feasibility. It will be important, however, to minimize, or at least account for, low-loss background scattering processes, such as Cherenkov radiation, which could potentially mask the identification of the spectral signatures. It will also be important to use a dose rate of beam electrons that respects the excitation lifetimes of the defects ($\sim$10–20 ns for NV^- and $\sim$1 ns for SiV^0) so as not to cause significant multiple excitations which may lead to their ionization.

The specific appearance and symmetries of the STEM-EELS maps in Figs. 5 and 9 are determined by the nature of the projected transition charges. Within the tight-binding approximations of Secs. IV A and V A, the transition charges for NV^- and SiV^0 can be written in terms of the dangling carbon bonds, so the maps in Figs. 5 and 9 can be interpreted as representations of these dangling bonds, as seen in projection.

Regarding the dependence of the NV^- and SiV^0 cross sections on orientation, we note that the cross section is determined largely by the transition charges' dipole moments. More specifically, partial cross sections are mainly determined by the component of these dipole moments lying perpendicular to the beam. For NV^-, the cross section is largest at [111] because at that orientation the dipole moments of $\bar{e}_x a_1(2)$ and $\bar{e}_y a_1(2)$ are both perpendicular to the beam. On rotating from [111] to [11$\bar{2}$], the relevant component of $\bar{e}_x a_1(2)$ is constant, but that of $\bar{e}_y a_1(2)$ decreases to zero, and hence the NV^- cross section decreases accordingly. The SiV^0 case is a bit more involved: At the [111] orientation, the perpendicular components of the four transition dipoles have equal magnitudes of $p_\perp/2$. On rotating from [111] to [11$\bar{2}$], the relevant dipole components of $\bar{e}_x^g e_x^u$ and $\bar{e}_y^g e_y^u$ both increase since $p_\parallel > p_\perp/2$ for this defect. This accounts for the increase in the SiV^0 cross section on rotating from [111] to [11$\bar{2}$].

We note that we have neglected the effect of phonons on the excitation of defect centers in this work. Phonons give rise to multiple peaks in excitation spectra, where each peak corresponds to the creation of a specific number of phonon quanta within the underlying electronic excitation. In a photoluminescence spectrum, the zero-phonon line sits at the upper edge of a sideband of lower-energy photons, representing the relatively shallower transitions from the zero-phonon electronic excited state to an n-phonon electronic ground state. In the EEL spectrum, the sideband will manifest at energies above the zero-phonon line, representing excitations from the zero-phonon electronic ground state to an n-phonon electronic excited state. But while luminescence and excitation are not entirely symmetric (phonon states differ for the excited and ground electronic states), the work of Alkauskas and coworkers [38,51] has convinced us that in either case phonons will spread the spectral intensity across multiple peaks while having little effect on the total spectral intensity.

Still, detectability prospects improve when the signal is confined to a narrow energy range. This is one way that SiV^0 might compete alongside NV^- as an experimental candidate. While the luminescence line shape for NV^- is contained mainly within an $\sim$0.4 eV window [38], at low temperatures SiV^0 emits primarily at its zero-phonon line [52]. However, these energy ranges may not translate directly to the EEL spectra. Electrons carry more momentum than photons, so one should expect more phonons to be created by electron beams and hence to see a slightly broader energy range in EEL spectra than in photoluminescence spectra. For unambiguous detection, one must have both an interaction cross section that is acceptably large and a spread of spectral intensities over a range that is acceptably small.

VII. CONCLUSIONS

We used density-functional theory and a Møller potential scattering formalism to calculate STEM-EELS spectral maps and plane-wave cross sections for two important defect centers in bulk diamond, namely, the NV^- center and the SiV^0 center. The calculations indicate that STEM-EELS should, in principle, be able to locate individual occurrences of these defects with a precision of around 1 nm, with plane-wave scattering cross sections of the order of 10^{-4} Å^2. The latter cross sections are similar to or greater than core-level EELS cross sections that have already enabled individual atoms to be located. Similar conclusions are likely to apply to important optically allowed transitions of other point defects. Thus we are optimistic that such individual point defects in bulk materials can be successfully probed using STEM-EELS. Many advanced materials applications utilize such point defects. Hence our results indicate that STEM-EELS could become an extremely valuable tool for the legion of physicists, chemists, and materials scientists for whom an understanding of the properties of such point defects is crucial.

APPENDIX: REAL-VALUED DFT WAVE FUNCTIONS

To connect with the tight-binding theory, the DFT wave functions can be made real valued by transformation. For nondegenerate wave functions, this requires only multiplication by an overall phase. But for degenerate wave functions, a unitary transformation is required, which corresponds to a

similarity transformation between irreducible representations (irreps) of the relevant point group. While general approaches exist for finding similarity transformations between irreps [53], we have developed a useful simplified approach. Here we provide details of this approach for the twofold-degenerate NV^- wave functions $e_{x/y}$ which form an E representation of the C_{3v} group.

The real wave functions $e_{x/y}$ that we seek form the following real 2×2 irrep of C_{3v}:

$$E = \begin{pmatrix} 1 & 0 \\ 0 & 1 \end{pmatrix}, \quad C_3 = \begin{pmatrix} -\frac{1}{2} & -\frac{\sqrt{3}}{2} \\ \frac{\sqrt{3}}{2} & -\frac{1}{2} \end{pmatrix}, \quad C_3^2 = \begin{pmatrix} -\frac{1}{2} & \frac{\sqrt{3}}{2} \\ -\frac{\sqrt{3}}{2} & -\frac{1}{2} \end{pmatrix},$$
$$\sigma_1 = \begin{pmatrix} -1 & 0 \\ 0 & 1 \end{pmatrix}, \quad \sigma_2 = \begin{pmatrix} \frac{1}{2} & \frac{\sqrt{3}}{2} \\ \frac{\sqrt{3}}{2} & -\frac{1}{2} \end{pmatrix}, \quad \sigma_3 = \begin{pmatrix} \frac{1}{2} & -\frac{\sqrt{3}}{2} \\ -\frac{\sqrt{3}}{2} & -\frac{1}{2} \end{pmatrix}, \tag{A1}$$

where C_3 represents the threefold rotation about the defect axis and $\sigma_{1,2,3}$ represent reflections through the planes defined by the symmetry axis and the carbon nuclei $C_{1,2,3}$ of Fig. 1. The matrix elements of the above representation have the general form $M_{ij} = \langle e_i|\hat{O}|e_j\rangle$, where $\hat{O}$ is a symmetry operation in the group and i and j take on the values x or y. Likewise, the matrix elements implied by the DFT wave functions e'_i have the general form $M'_{ij} = \langle e'_i|\hat{O}|e'_j\rangle$. To obtain the real-valued wave functions $e_{x/y}$ we must find a transformation matrix U such that

$$\begin{pmatrix} e''_x \\ e''_y \end{pmatrix} = U \begin{pmatrix} e'_x \\ e'_y \end{pmatrix}, \tag{A2}$$

where $e''_{x/y}$ differ from the desired wave functions $e_{x/y}$ at most by an overall phase, which can easily be corrected at the end of the procedure. The above U makes a backward similarity transformation between the M' representation and the M representation of Eq. (A1): $M = U^\dagger M' U$. Since a similarity transformation preserves eigenvalues, σ'_1 must have eigenvalues of ± 1 corresponding to orthonormal (column) eigenvectors $\hat{\mathbf{e}}_\pm$. By construction, the 2×2 matrix $U = (\hat{\mathbf{e}}_-, \delta\hat{\mathbf{e}}_+)$ will satisfy $\sigma_1 = U^\dagger \sigma'_1 U$ for any $|\delta| = 1$. One then can use another symmetry operator, such as $C_3 = U^\dagger C'_3 U$, to find a value of δ that will complete the construction of an appropriate U.

This approach is extended fairly easily to the degenerate SiV^0 wave functions $e^g_{x/y}$ and $e^u_{x/y}$, for which the relevant point group is D_{3d}.

[1] P. M. Voyles, J. L. Grazul, and D. A. Muller, Ultramicroscopy **96**, 251 (2003).
[2] P. M. Voyles, D. A. Muller, J. L. Grazul, P. H. Citrin, and H.-J. L. Gossmann, Nature **416**, 826 (2002).
[3] A. A. Gunawan, K. A. Mkhoyan, A. W. Wills, M. G. Thomas, and D. J. Norris, Nano Lett. **11**, 5553 (2011).
[4] A. Mittal and K. A. Mkhoyan, Ultramicroscopy **111**, 1101 (2011).
[5] P. Phillips, M. D. Graef, L. Kovarik, A. Agrawal, W. Windl, and M. Mills, Ultramicroscopy **116**, 47 (2012).
[6] J. M. Johnson, S. Im, W. Windl, and J. Hwang, Ultramicroscopy **172**, 17 (2017).
[7] R. M. Stroud, T. C. Lovejoy, M. Falke, N. D. Bassim, G. J. Corbin, N. Dellby, P. Hrncirik, A. Kaeppel, M. Noack, W. Hahn, M. Rohde, and O. L. Krivanek, Appl. Phys. Lett. **108**, 163101 (2016).
[8] Z. Liu, K. Suenaga, Z. Wang, Z. Shi, E. Okunishi, and S. Iijima, Nat. Commun. **2**, 213 (2011).
[9] R. Senga and K. Suenaga, Nat. Commun. **6**, 7943 (2015).
[10] S. L. Y. Chang, A. S. Barnard, C. Dwyer, C. B. Boothroyd, R. K. Hocking, E. Ōsawa, and R. J. Nicholls, Nanoscale **8**, 10548 (2016).
[11] S. Wang, K. March, F. A. Ponce, and P. Rez, Phys. Rev. B **99**, 115312 (2019).
[12] M. W. Doherty, N. B. Manson, P. Delaney, F. Jelezko, J. Wrachtrup, and L. C. Hollenberg, Phys. Rep. **528**, 1 (2013).
[13] J. R. Weber, W. F. Koehl, J. B. Varley, A. Janotti, B. B. Buckley, C. G. Van de Walle, and D. D. Awschalom, Proc. Natl. Acad. Sci. U.S.A. **107**, 8513 (2010).
[14] P. Neumann, N. Mizuochi, F. Rempp, P. Hemmer, H. Watanabe, S. Yamasaki, V. Jacques, T. Gaebel, F. Jelezko, and J. Wrachtrup, Science **320**, 1326 (2008).
[15] L. J. Rogers, K. D. Jahnke, M. H. Metsch, A. Sipahigil, J. M. Binder, T. Teraji, H. Sumiya, J. Isoya, M. D. Lukin, P. Hemmer, and F. Jelezko, Phys. Rev. Lett. **113**, 263602 (2014).
[16] S. Dhomkar, P. R. Zangara, J. Henshaw, and C. A. Meriles, Phys. Rev. Lett. **120**, 117401 (2018).
[17] B. L. Green, S. Mottishaw, B. G. Breeze, A. M. Edmonds, U. F. S. D'Haenens-Johansson, M. W. Doherty, S. D. Williams, D. J. Twitchen, and M. E. Newton, Phys. Rev. Lett. **119**, 096402 (2017).
[18] C. Dwyer, Ultramicroscopy **104**, 141 (2005).
[19] C. Dwyer, Ultramicroscopy **151**, 68 (2015).
[20] C. Dwyer, Phys. Rev. B **96**, 224102 (2017).
[21] G. Kresse and J. Hafner, Phys. Rev. B **47**, 558 (1993).
[22] G. Kresse and J. Hafner, Phys. Rev. B **49**, 14251 (1994).
[23] G. Kresse and J. Furthmüller, Comput. Mater. Sci. **6**, 15 (1996).
[24] G. Kresse and J. Furthmüller, Phys. Rev. B **54**, 11169 (1996).
[25] P. E. Blöchl, Phys. Rev. B **50**, 17953 (1994).
[26] G. Kresse and D. Joubert, Phys. Rev. B **59**, 1758 (1999).
[27] J. P. Perdew, K. Burke, and M. Ernzerhof, Phys. Rev. Lett. **77**, 3865 (1996).
[28] R. M. Feenstra, N. Srivastava, Q. Gao, M. Widom, B. Diaconescu, T. Ohta, G. L. Kellogg, J. T. Robinson, and I. V. Vlassiouk, Phys. Rev. B **87**, 041406(R) (2013).
[29] L. Zhang, R. Erni, J. Verbeeck, and G. Van Tendeloo, Phys. Rev. B **77**, 195119 (2008).
[30] K. Momma and F. Izumi, J. Appl. Crystallogr. **44**, 1272 (2011).
[31] A. Lenef and S. C. Rand, Phys. Rev. B **53**, 13441 (1996).
[32] N. B. Manson, J. P. Harrison, and M. J. Sellars, Phys. Rev. B **74**, 104303 (2006).
[33] J. R. Maze, A. Gali, E. Togan, Y. Chu, A. Trifonov, E. Kaxiras, and M. D. Lukin, New J. Phys. **13**, 025025 (2011).
[34] A. Gali, E. Janzén, P. Deák, G. Kresse, and E. Kaxiras, Phys. Rev. Lett. **103**, 186404 (2009).

[35] A. Gali, M. Fyta, and E. Kaxiras, Phys. Rev. B **77**, 155206 (2008).
[36] J. A. Larsson and P. Delaney, Phys. Rev. B **77**, 165201 (2008).
[37] B. Deng, R. Q. Zhang, and X. Q. Shi, Sci. Rep. **4**, 5144 (2014).
[38] A. Alkauskas, B. B. Buckley, D. D. Awschalom, and C. G. V. de Walle, New J. Phys. **16**, 073026 (2014).
[39] T. Plakhotnik, M. W. Doherty, and N. B. Manson, Phys. Rev. B **92**, 081203(R) (2015).
[40] J. Hertkorn, J. Wrachtrup, and M. Fyta, Eur. Phys. J.: Spec. Top. **227**, 1591 (2019).
[41] J. P. Goss, R. Jones, S. J. Breuer, P. R. Briddon, and S. Öberg, Phys. Rev. Lett. **77**, 3041 (1996).
[42] S. S. Moliver, Tech. Phys. **48**, 1449 (2003).
[43] A. Gali and J. R. Maze, Phys. Rev. B **88**, 235205 (2013).
[44] C. Hepp, T. Müller, V. Waselowski, J. N. Becker, B. Pingault, H. Sternschulte, D. Steinmüller-Nethl, A. Gali, J. R. Maze, M. Atatüre, and C. Becher, Phys. Rev. Lett. **112**, 036405 (2014).
[45] B. L. Green, M. W. Doherty, E. Nako, N. B. Manson, U. F. S. D'Haenens-Johansson, S. D. Williams, D. J. Twitchen, and M. E. Newton, Phys. Rev. B **99**, 161112(R) (2019).
[46] U. F. S. D'Haenens-Johansson, A. M. Edmonds, B. L. Green, M. E. Newton, G. Davies, P. M. Martineau, R. U. A. Khan, and D. J. Twitchen, Phys. Rev. B **84**, 245208 (2011).
[47] T. Mittiga, S. Hsieh, C. Zu, B. Kobrin, F. Machado, P. Bhattacharyya, N. Z. Rui, A. Jarmola, S. Choi, D. Budker, and N. Y. Yao, Phys. Rev. Lett. **121**, 246402 (2018).
[48] C. Dwyer, Phys. Rev. B **89**, 054103 (2014).
[49] M. Varela, M. P. Oxley, W. Luo, J. Tao, M. Watanabe, A. R. Lupini, S. T. Pantelides, and S. J. Pennycook, Phys. Rev. B **79**, 085117 (2009).
[50] Q. M. Ramasse, C. R. Seabourne, D.-M. Kepaptsoglou, R. Zan, U. Bangert, and A. J. Scott, Nano Lett. **13**, 4989 (2013).
[51] A. Alkauskas, M. D. McCluskey, and C. G. Van de Walle, J. Appl. Phys. **119**, 181101 (2016).
[52] B. C. Rose, D. Huang, Z.-H. Zhang, P. Stevenson, A. M. Tyryshkin, S. Sangtawesin, S. Srinivasan, L. Loudin, M. L. Markham, A. M. Edmonds, D. J. Twitchen, S. A. Lyon, and N. P. de Leon, Science **361**, 60 (2018).
[53] M. Mozrzymas, M. Studziński, and M. Horodecki, J. Phys. A **47**, 505203 (2014).